Journal of Water Process Engineering 55 (2023) 104253

Contents lists available at ScienceDirect

Journal of Water Process Engineering

journal homepage: www.elsevier.com/locate/jwpe

Phosphate recovery from wastewater by rapid adsorption-desorption enrichment over UiO-66@melamine sponge composites

Junna Yan [a,1], Mengyu Ma [a,1], Bo Zhao [b], Feihu Li [a,b,*]

[a] Collaborative Innovation Center of Atmospheric Environment and Equipment Technology, Jiangsu Key Laboratory of Atmospheric Environment Monitoring and Pollution Control, School of Environmental Science and Engineering, Nanjing University of Information Science and Technology, 219 Ningliu Road, Nanjing 210044, China

[b] NUIST Reading Academy, Nanjing University of Information Science and Technology, 219 Ningliu Road, Nanjing 210044, China

ARTICLE INFO

Keywords:
Metal-organic frameworks
UiO-66
Phosphorus recovery
Water purification

ABSTRACT

Excessive discharge of phosphorus (P) to natural watercourses not only causes eutrophication of water bodies but also results in the loss of P resources. P-containing wastewater is a crucial secondary P resource. Zirconium-based metal-organic frameworks (MOFs), particularly UiO-66 has been shown great promise in efficiently capturing P from water. In this study, a group of UiO-66@sponge composites was prepared by a facile layer-by-layer in-situ growth approach using melamine sponge (MS) as scaffolds. The as-prepared UiO-66@sponge composites exhibit high chemical and dimensional stability when used as adsorbents for reclaiming P from wastewater. Batch adsorption results show that one UiO-66@sponge composite exhibited the highest phosphorus adsorption capacity of 83.55 mg g^{-1} at pH 6.0, outperforming most other UiO-66 adsorbents under environmentally relevant conditions. The intrinsic mechanical flexibility and chemical stability of these UiO-66@sponge composites enable us to efficiently enrich phosphorus from a dilute solution by a rapid adsorption-desorption operation. This work provides a promising strategy to integrate MOFs with dimensionally stable and flexible sponges for rapid adsorption and recovery of phosphate from wastewater and could be potentially expanded to the recovery of other value-added or technology-critical elements from waste streams.

1. Introduction

Phosphorus (P) is an essential element for biological growth, but its excessive discharge can lead to serious environmental concerns [1]. Phosphorus in nature occurs mainly in the form of phosphate ore, which is a non-renewable resource that is currently being depleted at an alarming rate [2,3]. As most of the phosphorus is released into the environment through wastewater, which is likely to result in eutrophication of the receiving water bodies (e.g., lakes, reservoirs), destruction of aquatic ecosystems, deterioration of water quality, and threatening drinking water safety [1,2,4]. From the perspective of circular economy, phosphorus-containing wastewater is also an important secondary phosphorus resource. The research and development of phosphorus recovery techniques from wastewater can not only effectively solve the water pollution problem caused by phosphorus discharge, but also avoid the one-way loss of phosphorus resources, which is therefore of great significance for the sustainability of our society [1,5].

Among the various phosphorus removal and recovery technologies, adsorption plays an important role because of its simplicity of operation, cost-effectiveness, and wide adaptability to various effluents [6,7]. In the attempts to develop effective adsorbents for phosphate uptake, a range of materials such as graphene [8], metal (hydrated)oxides [9,10] and metal-organic frameworks (MOFs) [11–14] have been extensively explored for phosphate adsorption. It is well-established that MOFs have a high affinity toward phosphate due to the strong bonding between the phosphate anion and the metal center [11–13,15]. Water-stable MOFs such as UiO-66, NU-1000, and MIL-101 have been widely used as adsorbents for phosphate removal and recovery [16–20]. For instance, Guan et al. investigated the adsorption of phosphate from acidified urine by four UiO-66 and found that zirconium content, pore size, and crystallinity were the main factors affecting the adsorption process [21]. Xie and colleagues explored the P adsorption behavior of two iron-based

* Corresponding author at: School of Environmental Science and Engineering, Nanjing University of Information Science and Technology, 219 Ningliu Road, Nanjing 210044, China.
E-mail address: fhli@nuist.edu.cn (F. Li).
[1] These authors contributed equally to this work.

https://doi.org/10.1016/j.jwpe.2023.104253
Received 10 August 2023; Received in revised form 30 August 2023; Accepted 2 September 2023

MOFs, i.e., MIL-101(Fe) and NH_2-MIL-101(Fe), and observed that the grafting amine groups to MIL-101 demonstrated a higher affinity toward phosphate [22]. Such enhancement in affinity by the amine group was also observed in Zr-based UiO-66 adsorbents elsewhere [23]. However, these micro- or nano-sized MOFs are usually in powder form and therefore tend to agglomerate in solution, making them difficult to reclaim from aqueous systems [19]. Moreover, the decomposition of such MOFs can lead to the release of many finer particles and thus may pose potential toxic impacts on aquatic organisms in the receiving water body [24,25]. In addition, their poor reusability largely limits their practical application [24,26].

To address the above issues and the shortcomings of powdered adsorbents, implanting or anchoring such powders onto porous rigid scaffolds (e.g., biochar, ion exchange resins, etc.) offers a very promising solution [10,27–29]. However, these rigid supports are often difficult to synthesize, tend to wear out after long-term operation, and thus are not cost-effective as expected [29]. In contrast, melamine sponge (MS) has the advantages of low density, low cost, good flexibility, adjustable surface properties, and high chemical stability in diverse environments, making it an ideal macroporous scaffold for the preparation of various functional materials [28,30–32]. For example, Liu et al. developed an aluminum functionalized MS composite as a cost-effective adsorbent for phosphate, which can be separated directly from the solution after adsorption and exhibited good recoverability [28]. More recently, both iron (hydroxyl)oxide-loaded MS (FeOOH@MS) and NH_2-MIL-101(Fe/Ce)-anchored MS composites were prepared for P capture from water, respectively [19,32], and both adsorbents demonstrated good performance and great feasibility in practical applications. As mentioned above, UiO-66 has been extensively investigated as an adsorbent for phosphorus removal [18,21,23,33], but the feasibility of anchoring such MOFs within MS scaffolds for phosphorus capture from wastewater has not been explored so far.

Inspired by the aforementioned studies, we herein present a facile layer-by-layer (LbL) in-situ growth approach to prepare UiO-66-anchored MS composites (denoted as UiO-66@sponge) for capturing P from both synthetic and real wastewater under environmentally relevant conditions. The adsorption performance of such UiO-66@sponge composites toward P has been comprehensively evaluated via batch adsorption tests. In particular, benefitting from the mechanical flexibility of these UiO-66@sponge composites, a rapid adsorption-desorption enrichment operation within a syringe was used to recover phosphate from a low-P solution. Moreover, the mechanism of phosphate uptake over UiO-66@sponge has been illustrated using various molecular spectroscopic techniques. This work presents a promising platform approach to integrate MOFs with macroporous elastic scaffolds for rapid and efficient recovery of P from wastewater. This strategy is hopefully to be expanded to capture and reclaim other elements of interest from waste streams, offering a new promising avenue to urban mining.

2. Materials and methods

2.1. Chemicals

Zirconium tetrachloride ($ZrCl_4$, ≥98 %), dopamine hydrochloride (DA, 98 %), and heptane (98 %) were purchased from Aladdin Biochemical Technology Co., Ltd. (Shanghai, China). Monopotassium phosphate (KH_2PO_4, ≥99.0 %), and terephthalic acid (TPA, 99.9 %) were obtained from Macklin Biochemical Co., Ltd. (Shanghai, China). *N*, *N*-dimethylformamide (DMF, ≥99.5 %), hydroxyl-terminated polydimethylsiloxane (PDMS, ≥98 %), and tetraethyl orthosilicate (TEOS, 99.9 %) were purchased from Sinopharm Chemical Reagent Co., Ltd. (Shanghai, China). All chemicals were used as received. Ultrapure water (18.2 MΩ·cm, 25 °C) was employed for preparing solutions.

2.2. Preparation of UiO-66@sponge composites

Before preparing UiO-66@sponge composites, the melamine sponge (MS) cubes with a size of 1 cm × 1 cm × 1 cm were soaked in a 5 M NaOH solution at 65 °C for 30 min, followed by washing with excessive deionized water and drying in a vacuum oven at 65 °C for 12 h. Using these clean MS cubes as scaffolds, the composites were then synthesized using a facile method illustrated in Fig. 1a. Briefly, the MS cubes were soaked in a 2 mg L^{-1} DA solution prepared by dissolving 1 mg of dopamine hydrochloride in a 250 mL of 10 mM Tris-HCl buffer (pH 8.5). This DA coating process lasted for 12 h to ensure a full self-polymerization of DA within the surface of MS scaffolds to form a polydopamine (PDA) film. Then, the PDA-coated MS (denoted as MS@PDA) was rinsed with deionized water and ethanol, followed by drying in a vacuum oven at room temperature for 24 h. Next, the MS cubes were alternately immersed in an ethanolic solution of $ZrCl_4$ (10 mM) for 15 min and then in an ethanolic solution of TPA (10 mM) for 30 min at room temperature (~25 °C) for anchoring of UiO-66 particulates within MS scaffolds via a layer-by-layer (LbL) in-situ growth approach. Between each in-situ growth step, the MS scaffolds were rinsed with ethanol for 10 min to remove excess reagent and dried in a nitrogen stream for 5 min. After 5, 10, and 20 cycles of in-situ growth, a fraction of the as-prepared cubes (denoted as UiO-66@PDA-5, UiO-66@PDA-10, and UiO-66@PDA-20, respectively) were collected, dried at room temperature and stored in a glass desiccator for further use.

Likewise, the PDMS-coated MS can be made by simply replacing the PDA solution with a pre-crosslinked PDMS solution prepared by dissolving 1 wt% of PDMS (viscosity = 20,000 mPa·s) and 0.1 wt% of TEOS in n-heptane. Following the same in-situ growth procedure, PDMS-based UiO-66@sponge composites (denoted as UiO-66@PDMS-5, UiO-66@PDMS-10, and UiO-66@PDMS-20, respectively) were prepared in sequence. For comparison, UiO-66@MS sponge composites were also prepared following the same procedure as UiO-22@PDA composites.

2.3. Characterization of adsorbents

X-ray diffraction (XRD) analysis was performed on an XRD-6100 diffractometer (Shimadzu, Japan) with Cu-Kα radiation. The tube voltage was 40 kV and the tube current was 30 mA, while the step size and the scanning rate were set to 0.02° and 5° min^{-1}, respectively. A DELTA DC 4000 analyzer (Olympus, USA) with soil mode was used for X-ray fluorescence spectroscopy (XRF) analysis. Fourier transform infrared (FT-IR) spectroscopy was recorded using the KBr pellet method on a Nicolet iS5 spectrometer (Thermo Fisher, USA). The microscopic morphology of the adsorbent was collected on an SU1510 scanning electron microscope (SEM, Hitachi, Japan) at a 1.5 kV acceleration voltage. X-ray photoelectron spectroscopy (XPS) analysis was performed on a PHI 5000 spectroscope (Versa Probe, UIVAC-PHI, Japan). The instrument is equipped with a monochromatized Al Kα X-ray source ($h\nu$ = 1486.6 eV). The C 1s binding energy (284.8 eV) is used for the calibration of the binding energy value of other elements. The contact angle of water droplets on the surface of both pristine and P-loaded UiO-66@sponge composites was also measured at room temperature using a CAM 200 optical contact angle meter (KSV, Finland).

2.4. Phosphate adsorption experiments

The stock solution of 1000 mg PO_4^{3-} L^{-1} (equivalent to 10.5 mM) was prepared by dissolving the desired amount of monopotassium phosphate in ultrapure water and stored in a refrigerator at 4 °C for further dilution. All the batch adsorption experiments were carried out in triplicate and at room temperature (approximately 25 °C). The pH effect experiments were performed in 20 mg PO_4^{3-} L^{-1} solutions with a constant adsorbent dosage of 1 g L^{-1} over the pH range of 4 to 10. The procedure was the same as described elsewhere [19]. The concentration of P was determined using a JH723PC visible spectrophotometer (Jinghua Instrument

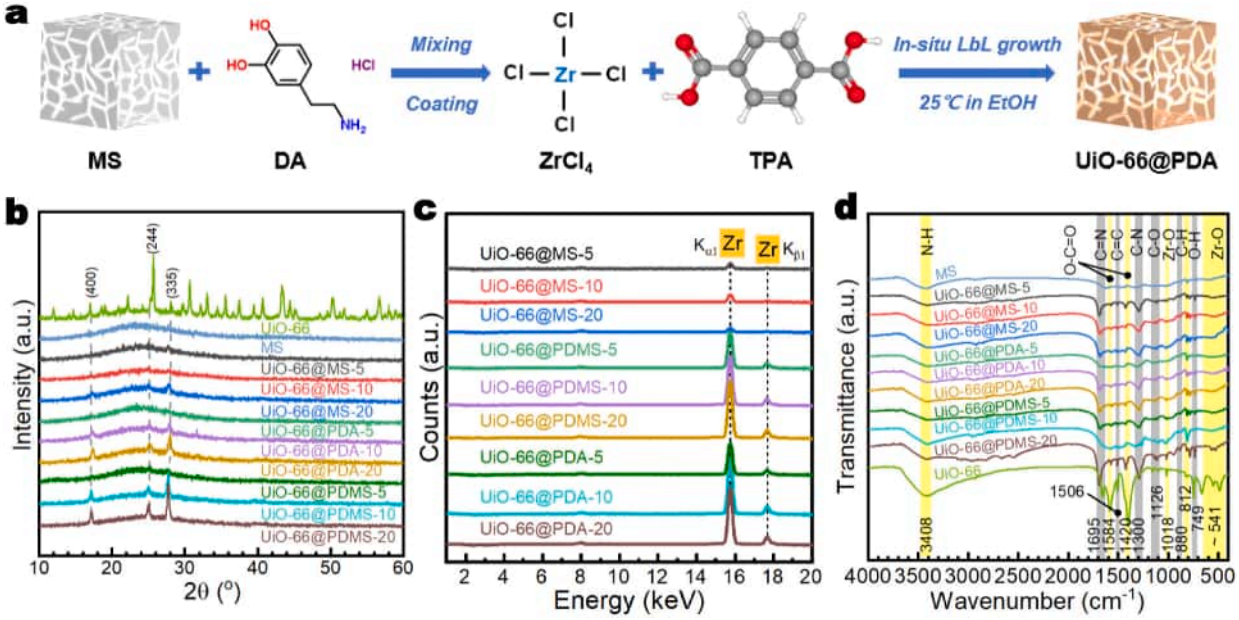

Fig. 1. (a) Schematic illustration of the preparation of UiO-66@sponge composites; (b) XRD patterns, (c) XRF spectra, and (d) FT-IR spectra of MS, UiO-66 and UiO-66@sponge composites.

Co. Ltd., China) according to the ascorbic acid method [34]. P adsorption capacity was calculated using the formula expressed below as Eq. (1):

$$Q = \frac{(C_0 - C_e) \times V}{m} \tag{1}$$

where Q denotes the adsorption capacity (mg PO_4^{3-} g^{-1}), m represents the adsorbent mass (g), C_0 indicates the original P concentration (mg PO_4^{3-} L^{-1}), C_e refers to the P concentration in solution after 24 h of adsorption when an equilibrium state was assumed to be reached, V stands for the total volume of solution (L).

According to the existing formulations for P adsorption on common inorganic adsorbents [6,17], the adsorption kinetics study was performed in 20 mg PO_4^{3-} L^{-1} solutions (pH = 6.0 ± 0.1). The adsorbent dosage was 1 g L^{-1} and the contact time ranged from 0 to 20 h. The experimental data were fitted with the pseudo-first order (Eq. (2)), pseudo-second order (Eq. (3)) and intraparticle diffusion (IPD, Eq. (4)) models formulated as follows:

$$ln(Q_e - Q_t) = lnQ_e - k_1 t \tag{2}$$

$$\frac{t}{Q_t} = \frac{1}{k_2 Q_e^2} + \frac{t}{Q_e} \tag{3}$$

$$Q_t = k_p t^{1/2} + C \tag{4}$$

where Q_t refers to the adsorption capacity at contact time t (h), Q_e denotes the adsorption capacity at equilibrium; k_1, k_2, and k_p stand for the pseudo-first, pseudo-second order, and IPD rate constants, respectively; C is a constant for any experiment in mg g^{-1}.

Similarly, in a group of solutions of original P concentration varying from 5 to 100 mg L^{-1} (pH = 6.0 ± 0.1), the adsorption isotherm experiments were performed in triplicate with a constant adsorbent dosage of 1 g L^{-1}. The contact time was set to 24 h assuming that adsorption equilibrium was reached. To fit the isotherm data, the Freundlich (Eq. (5)), Langmuir (Eq. (6)), and Sips models (Eq. (7)) shown below were applied:

$$Q_e = k_F C_e^{1/n} \tag{5}$$

$$Q_e = \frac{k_L Q_m C_e}{1 + K_L C_e} \tag{6}$$

$$Q_e = \frac{Q_m (k_S C_e)^n}{(1 + (k_S C_e)^n)} \tag{7}$$

where k_F (in (mg^{1-n} L^n) g^{-1}) and n denote the Friedrich constants, k_L refers to the Langmuir adsorption energy constant (L mg^{-1}), k_S indicates the Sips adsorption energy constant (L mg^{-1}) and Q_m refers to the theoretical maximum adsorption capacity (mg PO_4^{3-} g^{-1}).

2.5. Rapid adsorption-desorption recycling and enrichment tests

According to the same procedure outlined previously [35–37], our preliminary tests showed that 0.1 M NaOH solution provided optimum desorption efficiency. Therefore, 0.1 M NaOH solution was used as the eluent for rapid adsorption-desorption recycling tests. Both the simulated (P = 20 mg L^{-1}) and the real sewage (P = 13 mg L^{-1}, see Table S1) were used for testing. For the rapid adsorption-desorption test in a 10 mL syringe [19], UiO-66@PDA-10 and UiO-66@PDMS-10 of cylinders (Φ 15 mm, H 5.6 mm) were used. Briefly, the syringe with a piece of UiO-66@PDA-10 or UiO-66@PDMS-10 cylinder was imbued with 10 mL of P solution, followed by statical adsorption of 5 min before the solution was squeezed out. The P-loaded adsorbent was then regenerated with 5 mL of 0.1 M NaOH solution for 5 min, resulting in a P-enriched eluate and a regenerated adsorbent, which was then sequentially reused in the above adsorption-desorption cycle. For the adsorption-desorption recycling test, fresh NaOH solution was used for each desorption cycle, whereas the same NaOH solution was repeatedly used as eluent over 10 cycles in the case of adsorption-desorption enrichment testing.

3. Results and discussions

3.1. Characteristics of UiO-66@sponge composites

Fig. 1b shows the XRD patterns of UiO-66@MS as a function of the number of in-situ growth with both the UiO-66 powder and the MS scaffold as references. By comparison with the standard reflections of UiO-66 (the topmost green curve in Fig. 1b), it is clear that UiO-66

particulates can be anchored onto the surface of the MS scaffold by the layer-by-layer in-situ growth approach regardless of whether the MS scaffold has been precoated organically or not. It is recalled that the MS scaffold has been pretreated by 5 M NaOH before anchoring UiO-66. The resulting hydroxyl-terminated MS scaffold is beneficial to bond positive ions (e.g., Zr^{4+} ions), thus facilitating the nucleation and growth of UiO-66 particulates on its surface [31]. The intensities of three typical reflections, i.e., (400), (244), and (335) increased with the number of in-situ growth apparently, indicating the consecutive growth of the UiO-66 crystals. In addition, the diffusion reflections at 20–30° ascribed to the amorphous MS scaffold were observed in all UiO-66@sponge composites, validating the stability of the MS scaffold and thereby the feasibility of the LbL in-situ growth approach in preparing such composites. Note that the peak intensities of the organically coated MS scaffolds (i.e., UiO-66@PDA and UiO-66@PDMS series) are greater than those of the bare MS scaffold with the same number of in-situ growth, e.g., the intensity of (335) reflection declines in the order UiO-66@PDMS-10 > UiO-66@PDA-10 > UiO-66@MS-10. This observation indicates that both the PDMS and PDA coatings acted as the nucleation center for UiO-66 deposition and growth [38], thereof facilitating the anchoring and growing of UiO-66 particulates over the organically coated MS scaffolds. This enhancement in UiO-66 anchoring by organic-coating is further validated by the XRF spectra (Fig. 1c), showing much more Zr elements (the two principal K-shell emission lines) loading over the two organically coated MS scaffolds compared to the bare MS scaffolds.

FT-IR spectroscopy was used to analyze the evolution of surface functional groups of the MS scaffolds after UiO-66 anchoring and growth (Fig. 1d). The characteristic IR bands at 749, 812, 880, 1126, 1300, 1695, and 3414 cm^{-1} are associated with stretching vibrations of O—H, C—H, C—O, C—N, C═N, and N—H, respectively [39,40]. While the IR peaks at 1420 and 1584 cm^{-1} are attributable to the symmetric and asymmetric stretching vibrations of O—C═O, respectively [18]. The weak band at 1506 cm^{-1} is assignable to the stretching vibration of C═C in the benzene ring. The band at ~541 and 1018 cm^{-1} is the stretching vibration of the Zr—O bond in the UiO-66 framework [18]. Notably, there was no significant decrease in the intensity of the fingerprinted IR bands of the MS scaffold (e.g., band at 812 cm^{-1}, yellow shaded) after anchoring of UiO-66, further confirming the stability of the MS scaffolds and the feasibility of the LbL in-situ growth approach for preparing these UiO-66@sponge composites.

The microstructure and morphology of both the pristine MS and the UiO-66@sponge composites were characterized using scanning electron microscopy, and the results are shown in Fig. 2. SEM images (Fig. 2a) show that the pristine MS has a relatively smooth surface with a three-dimensional (3D) macroporous structure. These 3D skeletons can act as a platform and support for anchoring UiO-66 particulates. After anchoring and in-situ growth of UiO-66, the surfaces of these MS scaffolds were deposited with UiO-66 crystals of diverse sizes and shapes (yellow arrows, Fig. 2b–d), which has also been observed previously in cases of other MOFs [38]. Note that the original smooth sponge fibers became rough and bumpy after anchoring UiO-66, thereof endowing them with more active sites to capture the target P ions from water [19]. Additionally, all composites maintained the original 3D frameworks upon continuous alkaline washing, anchoring, and drying operations, implying the chemical and dimensional stability of the MS scaffold. It is noteworthy that, upon 10 cycles of successive in-situ growth, much more UiO-66 crystals were deposited over the surface of PDA-coated MS scaffolds, followed by those of PDMS-coated and bare MS scaffolds. This observation further confirms that PDA is an efficient nucleation center for MOFs [38] and also suggests that the UiO-66@PDA composite is likely to offer optimal performance for phosphorus adsorption.

3.2. Effect of pH on phosphorate adsorption

To screen the best composite adsorbent, all the as-prepared UiO-66@sponge composites were used for adsorption testing with an initial phosphate concentration of 20 mg PO_4^{3-} L^{-1} (pH = 6.0, adsorbent dosage = 1 g L^{-1}, T = 25 °C, contact time = 24 h), and the results are shown in Fig. 3a. Note that the group of UiO-66@PDA adsorbents (yellow shaded, Fig. 3a) outperformed the other two groups of adsorbents overall in capturing P from water, with UiO-66@PDA-10 showing the highest adsorption capacity (Q) of 15.77 mg g^{-1}. In contrast, the adsorption capacities of all UiO-66@MS adsorbents were <5 mg g^{-1}, validating the above speculation from the micromorphological results (Fig. 2b–d). Interestingly, the P adsorption capacities of both UiO-66@MS and UiO-66@PDMS increased monotonically with the number of in-situ growth clearly, whereas UiO-66@PDA exhibited a different trend of increasing first and then declining with the number of in-situ growth. A plausible explanation for this observation is that the surfaces of both the PDMS-coated and the bare MS scaffolds were partially covered by UiO-66 crystals after 10 cycles of in-situ growth (see Fig. 2b, d), and more crystals can be anchored upon continued in-situ growth, thereof leading to an increasing P adsorption capacity. However, the surface of UiO-66@PDA-10 was almost fully occupied (see Fig. 2c),

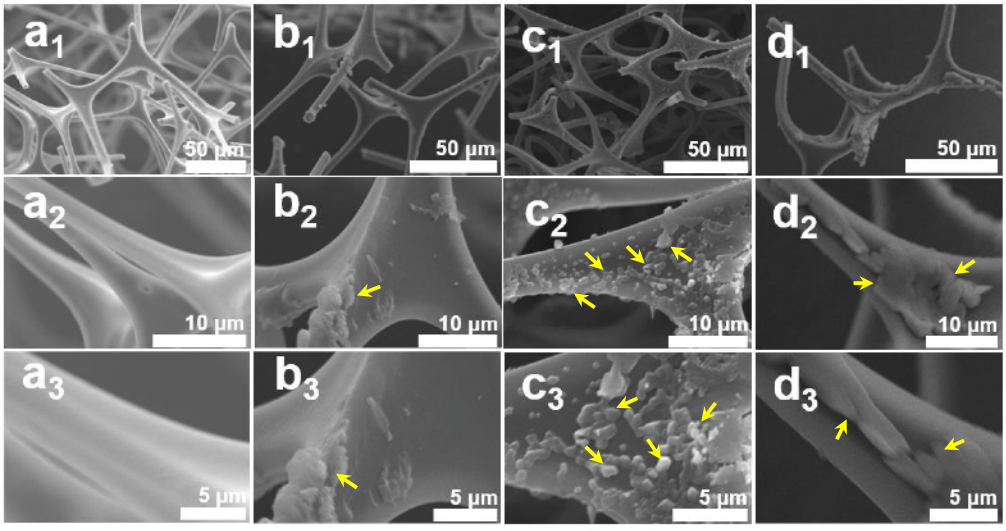

Fig. 2. SEM images of (a) MS scaffold, (b) UiO-66@MS-10, (c) UiO-66@PDA-10, and (d) UiO-66@PDMS-10. The yellow arrows indicate the UiO-66 particulates anchored on the MS surface. (For interpretation of the references to color in this figure legend, the reader is referred to the web version of this article.)

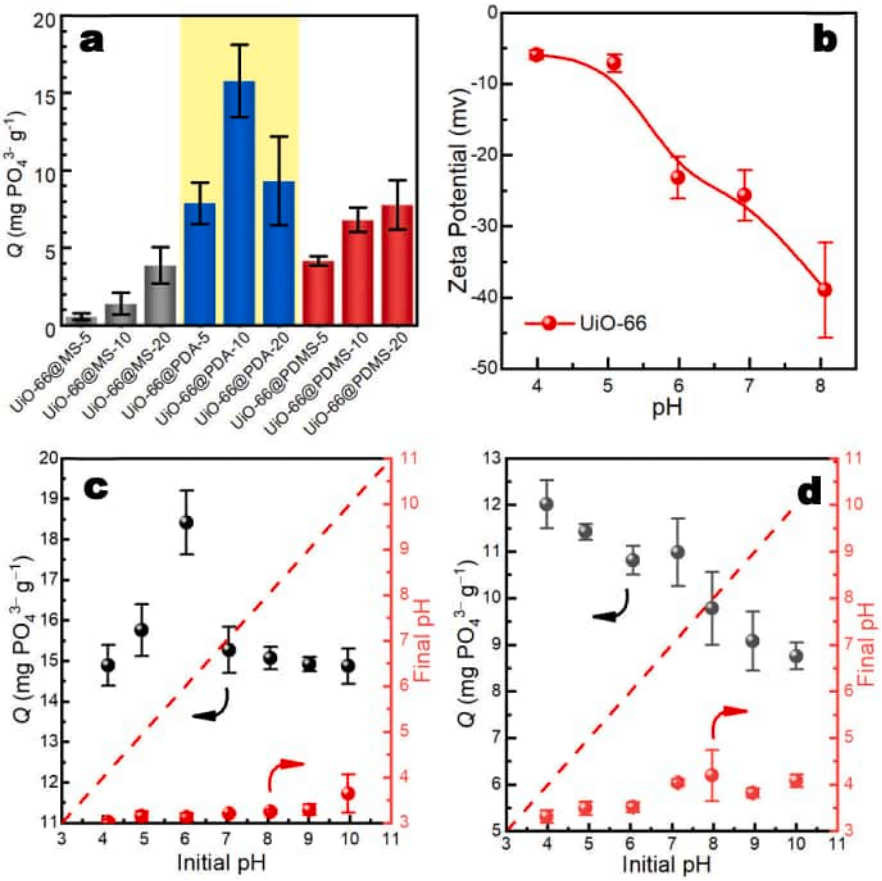

Fig. 3. (a) Comparison of P adsorption over different UiO-66@sponge composites with varying loadings of UiO-66; (b) the ζ potential profile of powder UiO-66; effects of initial solution pH on P adsorption and the corresponding pH profiles of (c) UiO-66@PDA-10 and (d) UiO-66@PDMS-10.

further anchoring UiO-66 may result in multilayer deposition with less exposure of active binding sites, thus suppressing its adsorption performance. Therefore, both UiO-66@PDA-10 and UiO-66@PDMS-10 were used for further evaluation of their adsorption performance toward phosphate.

Zeta (ζ) potential analysis on a Zetasizer Nano ZS90 meter (Malvern, UK) reveals that the surface of UiO-66 was negatively charged over the pH range tested (Fig. 3b), indicating the existence of intrinsic Coulomb repulsion between the composite adsorbents and adsorptive ions that are dominated in the anionic form over the pH range of 4–10 [41]. The effect of the initial solution pH on P adsorption and the final pH of the solution is shown in Fig. 3c–d. Notably, the final pH values deviated profoundly from the initial values by 1–6 units for both UiO-66@sponge composites (labeled by the red dashed line). This deviation of initial pH is likely due to the release of protons (H^+) from the ligand exchange reactions between the dominant $H_2PO_4^-$ ions and the protonated surface metal hydroxyls (i.e., >Zr–OH_2^+) of adsorbents at low pH region, and the moderate uptake of free hydroxyl ions from the solution by the UiO-66@sponge composites at high pH region [19,42].

Note that the adsorption capacity of UiO-66@PDA-10 for P showed a trend of increasing with pH over the pH range of 4 to 6, and then decreasing in pH 6–10. The UiO-66@PDMS-10, however, demonstrated a negative correlation of adsorption with pH, with Q decreasing from 12.0 mg g^{-1} at pH 4 to 8.8 mg g^{-1} at pH 10. Because dilute nitric acid was used to adjust the solution pH, quite a lot of nitrate ions were added in the suspension of adsorbent-adsorptive particularly in low pH region, which appears to compete with phosphate for the binding sites (see the following section). This seems to be a reasonable explanation of the P adsorption edge over UiO-66@PDA-10 at pH 4–6. However, further increasing the initial pH would turn the dominant phosphate species from $H_2PO_4^-$ to HPO_4^{2-} and PO_4^{3-} ions, which lowered phosphorus adsorption due to the enhanced Coulomb repulsion between more negatively charged ions and the negatively charged UiO-66@sponge composites (Fig. 3c–d). This observation is in good agreement with previous reports [23,43]. For UiO-66@PDMS-10, the P adsorption edge is likely to be solely governed by the increasing Coulomb repulsion with initial pH due to the hydrophobic surface of PDMS that is resistant to the adsorption of small molecules [44]. Nevertheless, both composites demonstrated a good adsorption capacity at pH 6, i.e., 18.4 and 10.8 mg g^{-1} for UiO-66@PDA-10 and UiO-66@PDMS-10, respectively. Therefore, the subsequent experiments were conducted at pH 6 where $H_2PO_4^-$ is the predominant phosphate species.

3.3. *Effect of coexisting species*

From a practical perspective, an excellent adsorbent should show good selectivity for the target species and be capable of resisting the interference of most complex coexisting species in the actual wastewater. It is well known that Cl^-, NO_3^-, SO_4^{2-}, HCO_3^-, and dissolved organic matter (DOM; e.g., humic acid, HA) species commonly found in actual wastewater may compete with phosphate for binding sites [6], thereby affecting the adsorption performance of the adsorbent for phosphate. Therefore, studying the effect of coexisting ions has been a common protocol for evaluating adsorbent selectivity toward a specific ion [42].

Competitive adsorption experiments of coexisting ions were performed separately with a mixture of phosphate (20 mg L^{-1}) and an individual competing species (0, 10, and 100 mg L^{-1}), and the results are shown in Fig. S1 (Supporting Information). All coexisting ions demonstrated competition with phosphate to some extent, with bicarbonate

ions (HCO_3^-) showing the greatest competition and nitrate ions the least for both composites. Specifically, the coexistence of HCO_3^- significantly affected phosphate adsorption, especially at high concentrations. For example, UiO-66@PDA-10 showed a decrease in Q from 16.51 to 6.19 mg g^{-1} in the presence of 100 mg L^{-1} of HCO_3^-. Likewise, the presence of such a high concentration of HCO_3^- also led to a reduction in Q of UiO-66@PDMS-10 by 75 %. It is believed that the competing ions often exhibited affinity to the binding sites through ligand exchange and the Coulomb attraction, thereof decreasing the uptake of P [18,26]. Also, HA shows a remarkable inhibition in phosphate adsorption, and the adsorption capacities of UiO-66@PDA-10 and UiO-66@PDMS-10 were decreased by 42.7 % and 48.9 %, respectively in the presence of 100 mg L^{-1} of HA. This is likely since HA can interact with surface >Zr-OH groups to form stable complexes, which in turn results in a decrease in binding sites for phosphate [45].

3.4. Adsorption kinetics

Intuitively, the adsorption kinetic experimental data (Q) of both the UiO-66@PDA-10 and the UiO-66@PDMS-10 composites (gray and red balls) showed a clear logarithmic relationship with the contact time (Fig. 4a–c). Specifically, P adsorption on both UiO-66@sponge composites was initially rapid (i.e., within the first 1 h) followed by slow reactions over the next few hours and beyond. For instance, the Q of UiO-66@PDA-10 increased from 0 to 14.8 mg g^{-1} as the contact time increased from 0 to 1 h, while further increasing the contact time to 20 h only led to an increase in Q by 1.7 mg g^{-1} (11.5 %). A similar trend was observed for UiO-66@PDMS-10 as well. Such adsorption behavior is termed a biphasic process, in which the rapid adsorption step is ascribed to chemical reaction and film diffusion processes, with a great large portion of the adsorption occurring within this rapid process [46].

To describe the adsorption behavior of P on both UiO-66@sponge composites, pseudo first-, second-order, and intraparticle diffusion models were employed to fit the experimental data. The best-fit kinetic parameters and the fitted curves are presented in Tables S2–S3 and Fig. 4a–c, respectively. The pseudo-first- and second-order kinetic models are suitable for describing the adsorption processes at controlled rates of physisorption and chemisorption, respectively [47]. Note that the pseudo-second-order kinetic model demonstrated larger correlation coefficients, R^2 (0.955 and 9.935 for UiO-66@PDA-10, and UiO-66@PDMS-10, respectively) compared to the pseudo-first-order kinetic model (Tables S2). Additionally, the adsorption capacity values at a presumed equilibrium state (Q_e) calculated by the pseudo-second-order model (i.e., 15.83 and 7.89 mg g^{-1} for UiO-66@PDA-10, and UiO-66@PDMS-10, respectively) were in general agreement with the actual Q values (i.e., 16.51 and 9.91 mg g^{-1}), confirming that the pseudo-second-order kinetic model is better to describe P adsorption phenomenon over both UiO-66@sponge composites compared to the pseudo-first-order model. Collectively, it is reasonable to speculate that phosphate adsorption on both UiO-66@sponge composites was controlled by a chemisorption process [18].

It is noteworthy that the intraparticle diffusion model for phosphate adsorption of both UiO-66@PDA-10 and UiO-66@PDMS-10 is nonlinear over the whole time range, and the obtained plots present multi-collinearity with an initial linear part followed by an intermediate linear part and a plateau (Fig. 4c), indicating that two or more steps occur in the adsorption process [48]. The P adsorption process on both composites can be divided into three stages (labeled with numbers in Fig. 4c). The first stage is external surface adsorption, in which intraparticle diffusion is not the only rate-controlling process and may involve other mechanisms such as initial external mass transfer or chemical reactions [49]. The second stage is the gradual adsorption stage. The last stage is the equilibrium adsorption stage, where intraparticle diffusion starts to slow down due to the decrease in phosphate concentration and the occupation of the binding sites of the adsorbent. The multicollinearity of the curves indicates that surface adsorption and

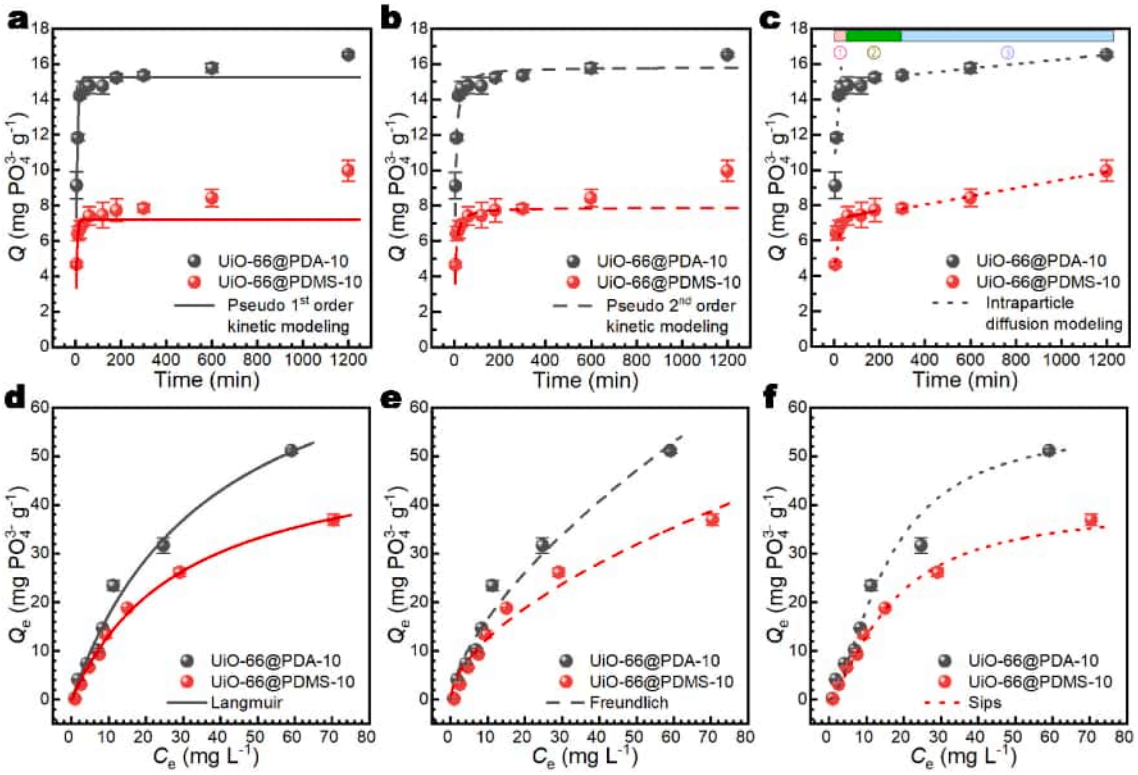

Fig. 4. Adsorption kinetics of P onto UiO-66@sponge composites with (a) pseudo-first-order kinetic modeling, (b) pseudo-second-order kinetic modeling, and (c) intraparticle diffusion modeling (adsorbent dosage = 1 g L^{-1}, P concentration = 20 mg PO_4^{3-} L^{-1}, T = 25 °C); adsorption isotherms of P onto UiO-66@sponge composites with (d) Langmuir model fitting, (e) Freundlich model fitting and (e) Sips model fitting (adsorbent dosage = 1 g L^{-1}, T = 25 °C, contact time = 24 h).

intraparticle diffusion occur simultaneously [49]. Phosphate is often initially adsorbed on the outer surface of the adsorbent, then migrates slowly into the particles by surface or intraparticle diffusion, and finally is retained within the pores. The best-fit intraparticle diffusion rate constants k and C are tabulated in Table S3. Note that UiO-66@PDA-10 showed a larger C value than UiO-66@PDMS-10, implying better intraparticle diffusion performance and thereof superior P adsorption behavior in UiO-66@PDA-10 compared to UiO-66@PDMS-10 [43].

3.5. Adsorption isotherms

To investigate the interaction between P species and adsorbents and estimate the adsorption capacity of adsorbents, Freundlich, Langmuir, and Sips models are applied to the equilibrium adsorption data. The best-fit isotherm parameters and the relevant correlation coefficients (R^2) are tabulated in Table S4, and the fitted plots are depicted in Fig. 4d–f. Note that both composites showed an increased Q as the equilibrium P concentration (C_e) increased, which is a typical L-shaped isotherm and indicative of a higher affinity of both adsorbents for P at low concentrations [50]. Clearly, UiO-66@PDA-10 demonstrated a quite higher uptake for P compared to UiO-66@PDMS-10, which is likely due to the intrinsic difference between the two coatings — PDA and PDMS — since PDA has a strong affinity for P, whereas PDMS does not [51].

In terms of the correlation coefficient values ($R^2 \geq 0.9$, Table S4), all three models, Langmuir, Freundlich, and Sips, appear to describe the adsorption isotherm experimental data well (see Fig. 4d–f). However, R^2 values obtained from the Langmuir equation are much closer to 1 compared to other models, suggesting that the Langmuir model is more appropriate to define the adsorption isotherm data. Since the Langmuir equation is based on an assumption of monolayer adsorption [50], the P adsorption processes on both composites are likely to proceed in a monolayer manner. The maximum adsorption capacity (Q_m) values calculated by the Langmuir equation (Eq. 6) are 83.55 and 53.13 mg g^{-1} for UiO-66@PDA-10 and UiO-66@PDMS-10, respectively (Table 1). Theoretically, the maximum P adsorption capacity of the pristine MS scaffold (i.e., 17.32 mg g^{-1}) has been significantly increased by about 5-fold by surface coating of PDA and subsequent anchoring of UiO-66, thereof demonstrating the feasibility and effectiveness of this LbL in-situ growth strategy. More importantly, in terms of maximum adsorption capacity under environmentally relevant conditions, both of our UiO-66@sponge composites outperform most other UiO-66-based adsorbents in the literature in capturing phosphorus from water (Table 1), demonstrating the great promise of using such UiO-66@sponge adsorbents for efficient phosphorus removal and recovery.

3.6. Rapid adsorption-desorption recycling and enrichment performance

As shown in Fig. 5a, the P adsorption capacity of UiO-66@PDA-10 decreased by 10 % after five cycles of consecutive rapid adsorption-desorption operation in treating simulated effluent (P = 20 mg L^{-1}). Likewise, it was found that the corresponding desorption efficiency decreased from 69 % to 51 %. It is believed that the deterioration in both the adsorption and the desorption efficiencies is primarily due to the quite short operation duration (i.e., 5 min adsorption followed by 5 min desorption) [19]. A validation attempt to extend the adsorption-desorption operation to a total of 20 min showed that the adsorption efficiency has decreased from 89 % to 81 % (declined by 8.9 %). Hence, a tradeoff between recycling performance and adsorption-desorption operation duration is apparent, and a total of 10 min of rapid adsorption-desorption operation is adopted. When applying to the actual sludge dewatering liquid of the Nanjing Qiaobei Wastewater Treatment Plant with a complex composition (Table S1), UiO-66@PDA-10 showed a similar trend of both adsorption and desorption efficiencies (declined by 16.1 % of the adsorption efficiency versus 32.5 % of the desorption efficiency after 5 cycles of recycling operation, Fig. 5c). Equally, UiO-66@PDMS-10 demonstrated a comparable recycling performance (Fig. S2a, c) with previous reports of UiO-66-based adsorbents [17,33,43]. It is interesting to note that the P adsorption efficiency has been significantly improved in the case of treating actual sludge dewatering liquid, which is most likely due to the presence of quite a large amount of calcium (Ca^{2+}) and magnesium (Mg^{2+}) ions that can promote the removal of phosphate [52]. Collectively, both UiO-66@sponge adsorbents demonstrated good recyclability in treating either the simulated or the actual wastewater effluents regardless of its compositional complexity.

When the same NaOH solution is used repeatedly as an eluent to up-concentrate P from a dilute solution, a P-rich eluate can be obtained for further recovering P via struvite crystallization [37]. To this end, both UiO-66@sponge adsorbents were employed to enrich P from both simulated and actual wastewater. As shown in Fig. 5b, our results show that after 10 cycles of the enrichment operation, a P-rich eluate (P = 26.6 mg L^{-1}) was achieved with UiO-66@PDA-10 as the adsorbent, with an enrichment factor of 1.33 to the initial P concentration of the simulated wastewater (i.e., 20 mg L^{-1}). Equally, an enrichment factor of 1.31 was attained for enriching the actual sludge dewatering liquid (P = 13 mg L^{-1}) irrespective of its complex composition (Fig. 5d). In comparison, UiO-66@PDMS-10 demonstrated a slightly poor enrichment factor for both effluents, i.e., 1.11 for simulated effluent versus 1.27 for actual effluent (Fig. S2b, d). Moreover, no zirconium can be detected in both eluates by an Optima 8000 inductively coupled plasma optical emission spectrometer (ICP-OES, PerkinElmer, Inc., USA), indicating the chemical stability of these adsorbents. Additionally, the SEM images of both adsorbents after 10 cycles of rapid adsorption-desorption operation (Fig. S3) also verify their dimensional stability. However, applying this syringe-based adsorption-desorption operation on a full scale could be quite challenging currently. Nonetheless, in terms of the above merits of these UiO-66@sponge adsorbents, such rapid adsorption-desorption operation with these adsorbents is expected to be used in certain point-of-use (POU) scenarios, such as remediation of specific toxic spills.

Table 1
Comparison of maximum P adsorption capacity of UiO-66-based adsorbents.

Adsorbent ID	pH	Temperature (°C)	Adsorption capacity (mg PO_4^{3-} g^{-1})	Ref.
MFC@UiO-66	6.5	30	16.95	[43]
HCl-UiO-66	4.0	N.A.	53.30	[55]
straw@UiO-66	4.5	25	69.30	[33]
UiO-66	4.0	20	74.50	[21]
HP-UiO-66(Zr)	6.5	25	80.20	[20]
UiO-66	N.A.	20	85.00	[17]
UiO-66@PDA-10	6.0	20	83.55	This study
UiO-66@PDMS-10	6.0	25	53.13	This study

3.7. Adsorption mechanism

To illuminate the underlying mechanism of P adsorption, XRD, XRF, FT-IR, and XPS analyses were performed before and after P adsorption using UiO-66@PDA-10 as the adsorbent of interest. As shown in Fig. 6a, the XRD profile of UiO-66@PDA-10 remained essentially unaffected upon P adsorption, with three diffraction peaks of almost the same intensity and 2θ position, confirming the structural integrity of the adsorbent. Note that a weak peak at 2.01 keV ascribed to the $K_{\alpha 1}$-shell emission line of phosphorus was detected in the XRF spectrum of P-loaded adsorbent (blue curve, inset in Fig. 6b), indicative of the successful uptake of P on UiO-66@PDA-10. Additionally, the strength of infrared bands at 1695, 1584, 1420, and 743 cm^{-1} increased apparently, while the IR band at 1018 cm^{-1}, attributed to the overlap of both the stretching vibration of Zr—O bond and the antisymmetric stretching of phosphate, $\nu_3(PO_4)$ [37], was slightly enhanced upon P adsorption (Fig. 6c). The former observation indicates that the C═H, O—C═O, and O—H groups are involved in P adsorption, whereas the latter suggests

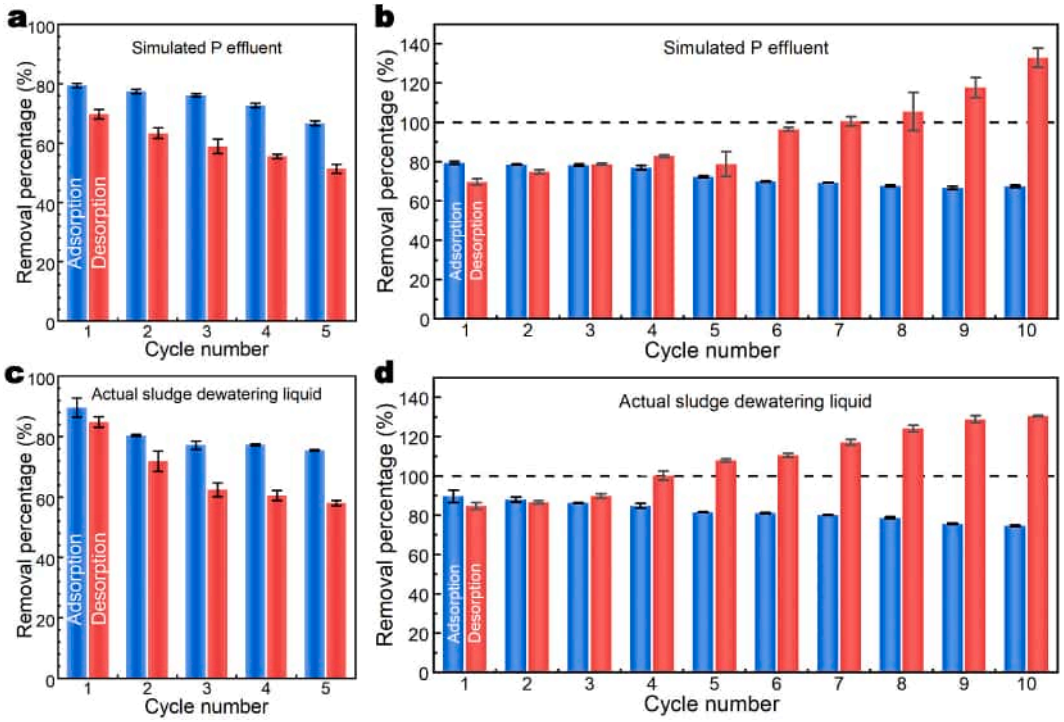

Fig. 5. Recycling (a) and enrichment (b) performance of UiO-66@PDA-10 for treating simulated P effluent (P = 20 mg L^{-1}), recycling (c) and enrichment performance (d) of UiO-66@PDA-10 for treating actual sludge dewatering liquid (P = 13 mg L^{-1}).

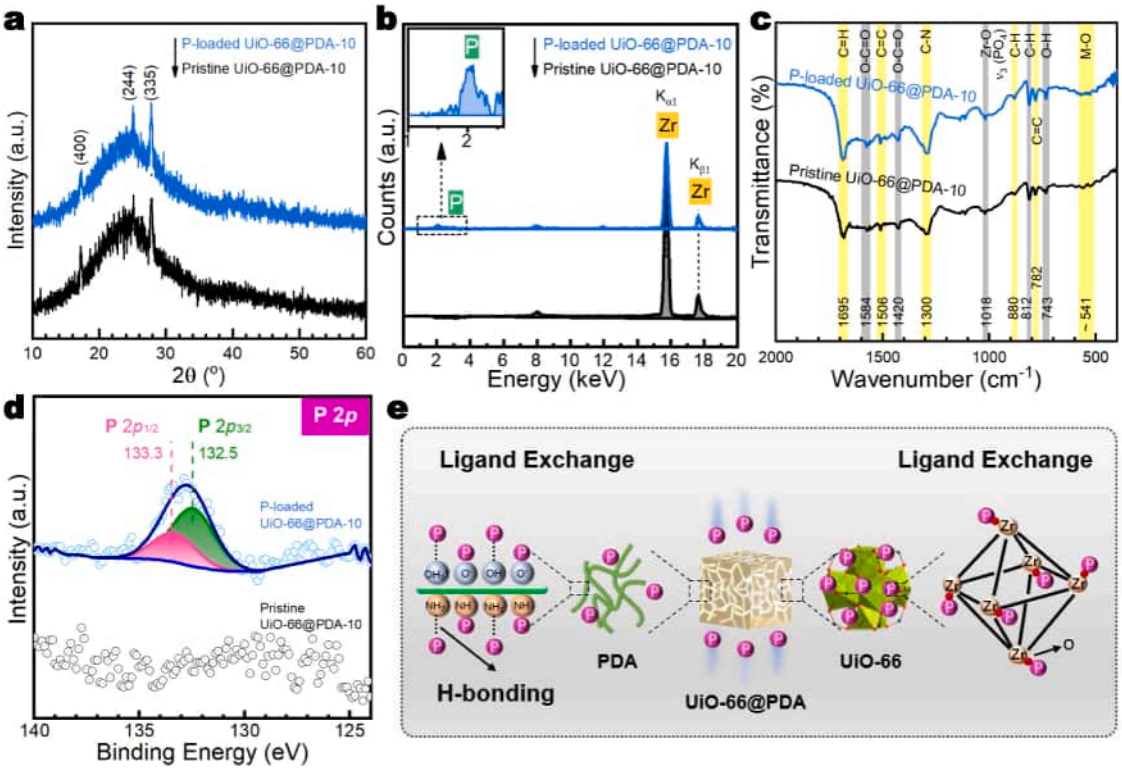

Fig. 6. (a) XRD patterns, (b) XRF spectra, (c) FT-IR spectra, and (d) P 2p XPS regions of UiO-66@PDA-10 before and after P adsorption; (e) schematic representation of the proposed P adsorption mechanism.

the success in complexing phosphate over the surface of UiO-66@PDA-10, most likely through the Zr—O—P coordination [53,54].

Moreover, XPS spectra also verified that P was successfully captured by UiO-66@PDA-10 according to the arising of a weak P 2p peak in the XPS survey spectrum (also see the inset atomic table in Fig. S4a) and the apparent splitting of the P 2p peak into two spin-orbit peaks centered at 133.3 eV ($2p_{1/2}$) and 132.5 eV ($2p_{3/2}$), respectively (Fig. 6d). Interestingly, the Zr 3d spin-orbit peaks shifted slightly to the high-energy

region and the fraction of oxygen species assignable to Zr—O—Zr or P—O increased from 4.3 to 6.7 % (~530.0 eV) after P adsorption (Fig. S4b, d), confirming the Zr— O— P coordination once again. Note that a slight increase in the N 1s peak intensity occurred upon P adsorption, implying the amino groups of PDA coating might be chemically involved in P uptake. In effect, it has been shown that the catechol and amino groups on the PDA coating have a strong affinity for phosphate [51]. To further visualize the impact of surface hydrophilicity or hydrophobicity of these adsorbents on P uptake, contact angle measurements were performed and the results are given in Fig. S5. Evidently, all UiO-66@sponge adsorbents were hydrophobic before P adsorption, with contact angles declining in the order UiO-66@PDMS-10 > UiO-66@MS-10 > UiO-66@PDA-10 (top row, Fig. S5). However, upon P adsorption, both UiO-66@MS-10 and UiO-66@PDA-10 became hydrophilic, while UiO-66@PDMS-10 remained hydrophobic due to the high hydrophobicity of the PDMS coating [44]. This could explain the relatively poor adsorption performance of UiO-66@PDMS-10 for phosphorus. Collectively, it is reasonable to attribute the principal mechanisms of P adsorption over UiO-66@PDA-10 to i) ligand exchange between phosphate and surface metal hydroxyl groups (i.e., >Zr-OH, >Zr-O^-), and ii) ligand exchange and hydrogen bonding between phosphate and surface groups of PDA coating (i.e., >NH, >C-OH, Fig. 6e).

4. Conclusions

In summary, zirconium-based MOFs — UiO-66 particulates have been successfully anchored within melamine sponge scaffolds precoated with PDA or PDMS using the layer-by-layer (LbL) in-situ growth method. The as-prepared UiO-66@PDA-10 and UiO-66@PDMS-10 show high chemical and dimensional stability when used as adsorbents for phosphate recovery from water. Batch adsorption results demonstrate that both UiO-66@sponge composites have high adsorption capacity for phosphate, with maximum phosphate adsorption capacities of 83.56 and 53.13 mg g^{-1} for UiO-66@PDA-10 and UiO-66@PDMS-10, respectively. Benefit from their inherent mechanical flexibility and chemical stability, these UiO-66@sponge composites can efficiently enrich phosphate from a dilute solution through a rapid adsorption-desorption operation, attaining an enrichment factor of 1.31 after 10 cycles of operation for an actual sludge dewatering liquid (P = 13 mg L^{-1}) regardless of its complex composition. This work could provide some valuable insight into the rational integration of MOF materials with sponge-like supports for reclaiming some value-added or technology-critical elements from waste streams, thereby facilitating further practical applications of such materials toward a sustainable society.

Declaration of competing interest

The authors declare that they have no known competing financial interests or personal relationships that could have appeared to influence the work reported in this paper.

Data availability

Data will be made available on request.

Acknowledgments

The work was partially supported by the National Natural Science Foundation of China (51002080), the Innovation Training Programme for Undergraduate Students of NUIST (XJDC202310300257) and of Reading Academy (RA 2023007). We would like to thank Dr. Fengying Li for her assistance in the XRF measurement.

Appendix A. Supplementary data

Supplementary data to this article can be found online at https://doi.org/10.1016/j.jwpe.2023.104253.

References

[1] E. Desmidt, K. Ghyselbrecht, Y. Zhang, L. Pinoy, B. Van der Bruggen, W. Verstraete, K. Rabaey, B. Meesschaert, Global phosphorus scarcity and full-scale P-recovery techniques: a review, Crit. Rev. Environ. Sci. Technol. 45 (2015) 336–384, https://doi.org/10.1080/10643389.2013.866531.
[2] C. Alewell, B. Ringeval, C. Ballabio, D.A. Robinson, P. Panagos, P. Borrelli, Global phosphorus shortage will be aggravated by soil erosion, Nat. Commun. 11 (2020) 4546, https://doi.org/10.1038/s41467-020-18326-7.
[3] A.R. Jupp, S. Beijer, G.C. Narain, W. Schipper, J.C. Slootweg, Phosphorus recovery and recycling — closing the loop, Chem. Soc. Rev. 50 (2021) 87–101, https://doi.org/10.1039/d0cs01150a.
[4] D.A. Vaccari, S.M. Powers, X. Liu, Demand-driven model for global phosphate rock suggests paths for phosphorus sustainability, Environ. Sci. Technol. 53 (2019) 10417–10425, https://doi.org/10.1021/acs.est.9b02464.
[5] B.E. Rittmann, B. Mayer, P. Westerhoff, M. Edwards, Capturing the lost phosphorus, Chemosphere 84 (2011) 846–853, https://doi.org/10.1016/j.chemosphere.2011.02.001.
[6] P. Loganathan, S. Vigneswaran, J. Kandasamy, N.S. Bolan, Removal and recovery of phosphate from water using sorption, Crit. Rev. Environ. Sci. Technol. 44 (2014) 847–907, https://doi.org/10.1080/10643389.2012.741311.
[7] T.C. Wang, W. Bury, D.A. Gomez-Gualdron, N.A. Vermeulen, J.E. Mondloch, P. Deria, K.N. Zhang, P.Z. Moghadam, A.A. Sarjeant, R.Q. Snurr, J.F. Stoddart, J. T. Hupp, O.K. Farha, Ultrahigh surface area zirconium MOFs and insights into the applicability of the BET theory, J. Am. Chem. Soc. 137 (2015) 3585–3591, https://doi.org/10.1021/ja512973b.
[8] D.K.L. Harijan, V. Chandra, Akaganeite nanorods decorated graphene oxide sheets for removal and recovery of aqueous phosphate, J. Water Process Eng. 19 (2017) 120–125, https://doi.org/10.1016/j.jwpe.2017.07.019.
[9] M.X. Li, J.Y. Liu, Y.F. Xu, G.R. Qian, Phosphate adsorption on metal oxides and metal hydroxides: a comparative review, Environ. Rev. 24 (2016) 319–332, https://doi.org/10.1139/er-2015-0080.
[10] R.T. Liu, L.N. Chi, X.Z. Wang, Y.M. Sui, Y. Wang, H. Arandiyan, Review of metal (hydr)oxide and other adsorptive materials for phosphate removal from water, J. Environ. Chem. Eng. 6 (2018) 5269–5286, https://doi.org/10.1016/j.jece.2018.08.008.
[11] S.J. Li, T. Lei, F. Jiang, M. Liu, Y.T. Wang, S.X. Wang, X.J. Yang, Tuning the morphology and adsorption capacity of Al-MIL-101 analogues with Fe^{3+} for phosphorus removal from water, J. Colloid Interface Sci. 560 (2020) 321–329, https://doi.org/10.1016/j.jcis.2019.10.077.
[12] R.Y. Zhou, J.X. Yu, R.A. Chi, Selective removal of phosphate from aqueous solution by MIL-101(Fe)/bagasse composite prepared through bagasse size control, Environ. Res. 188 (2020), 109817, https://doi.org/10.1016/j.envres.2020.109817.
[13] S. Khan, Q. Guan, Q. Liu, Z.W. Qin, B. Rasheed, X.X. Liang, X. Yang, Synthesis, modifications and applications of MILs metal-organic frameworks for environmental remediation: the cutting-edge review, Sci. Total Environ. 810 (2022), 152279, https://doi.org/10.1016/j.scitotenv.2021.152279.
[14] S. Rojas, P. Horcajada, Metal-organic frameworks for the removal of emerging organic contaminants in water, Chem. Rev. 120 (2020) 8378–8415, https://doi.org/10.1021/acs.chemrev.9b00797.
[15] M. Nehra, N. Dilbaghi, N.K. Singhal, A.A. Hassan, K.H. Kim, S. Kumar, Metal organic frameworks MIL-100(Fe) as an efficient adsorptive material for phosphate management, Environ. Res. 169 (2019) 229–236, https://doi.org/10.1016/j.envres.2018.11.013.
[16] L. Gonzalez, F.J. Carmona, N.M. Padial, J.A.R. Navarro, E. Barea, C.R. Maldonado, Dual removal and selective recovery of phosphate and an organophosphorus pesticide from water by a Zr-based metal-organic framework, Mater. Today Chem. 22 (2021), 100596, https://doi.org/10.1016/j.mtchem.2021.100596.
[17] K.Y.A. Lin, S.Y. Chen, A.P. Jochems, Zirconium-based metal organic frameworks: highly selective adsorbents for removal of phosphate from water and urine, Mater. Chem. Phys. 160 (2015) 168–176, https://doi.org/10.1016/j.matchemphys.2015.04.021.
[18] X.Y. Min, X. Wu, P.H. Shao, Z. Ren, L. Ding, X.B. Luo, Ultra-high capacity of lanthanum-doped UiO-66 for phosphate capture: unusual doping of lanthanum by the reduction of coordination number, Chem. Eng. J. 358 (2019) 321–330, https://doi.org/10.1016/j.cej.2018.10.043.
[19] J.N. Yan, M.Y. Ma, K.Y. Liu, Y. Bao, F.H. Li, Anchoring NH_2-MIL-101(Fe/Ce) within melamine sponge boosts rapid adsorption and recovery of phosphate from water, ACS ES&T Eng. 3 (2023) 467–478, https://doi.org/10.1021/acsestengg.2c00324.
[20] M.H. Li, Y.B. Liu, F. Li, C.S. Shen, Y.V. Kaneti, Y. Yamauchi, B. Yuliarto, B. Chen, C. C. Wang, Defect-rich hierarchical porous UiO-66(Zr) for tunable phosphate removal, Environ. Sci. Technol. 55 (2021) 13209–13218, https://doi.org/10.1021/acs.est.1c01723.
[21] T. Guan, X.D. Li, W.K. Fang, D.Y. Wu, Efficient removal of phosphate from acidified urine using UiO-66 metal-organic frameworks with varying functional groups, Appl. Surf. Sci. 501 (2020), 144074, https://doi.org/10.1016/j.apsusc.2019.144074.

[22] Q.Y. Xie, Y. Li, Z.L. Lv, H. Zhou, X.J. Yang, J. Chen, H. Guo, Effective adsorption and removal of phosphate from aqueous solutions and eutrophic water by Fe-based MOFs of MIL-101, Sci. Rep. 7 (2017) 3316, https://doi.org/10.1038/s41598-017-03526-x.
[23] X.T. Zhang, M.Y. Liu, R.P. Han, Adsorption of phosphate on UiO-66-NH_2 prepared by a green synthesis method, J. Environ. Chem. Eng. 9 (2021), 106672, https://doi.org/10.1016/j.jece.2021.106672.
[24] S. Dhaka, R. Kumar, A. Deep, M.B. Kurade, S.W. Ji, B.H. Jeon, Metal-organic frameworks (MOFs) for the removal of emerging contaminants from aquatic environments, Coord. Chem. Rev. 380 (2019) 330–352, https://doi.org/10.1016/j.ccr.2018.10.003.
[25] E. Moumen, L. Bazzi, S. El Hankari, Metal-organic frameworks and their composites for the adsorption and sensing of phosphate, Coord. Chem. Rev. 454 (2022), 214376, https://doi.org/10.1016/j.ccr.2021.214376.
[26] S.P. Zhang, J. Ding, D.Y. Tian, Incorporation of MIL-101 (Fe or Al) into chitosan hydrogel adsorbent for phosphate removal: performance and mechanism, J. Solid State Chem. 306 (2022), 122709, https://doi.org/10.1016/j.jssc.2021.122709.
[27] D.N.H. Tran, S. Kabiri, L.S. Wang, D. Losic, Engineered graphene-nanoparticle aerogel composites for efficient removal of phosphate from water, J. Mater. Chem. A 3 (2015) 6844–6852, https://doi.org/10.1039/c4ta06308b.
[28] R.T. Liu, J. Shen, X.J. He, L.N. Chi, X.Z. Wang, Efficient macroporous adsorbent for phosphate removal based on hydrate aluminum-functionalized melamine sponge, Chem. Eng. J. 421 (2021), 127848, https://doi.org/10.1016/j.cej.2020.127848.
[29] R. Xu, M.Y. Zhang, R.J.G. Mortimer, G. Pan, Enhanced phosphorus locking by novel lanthanum/aluminum-hydroxide composite: implications for eutrophication control, Environ. Sci. Technol. 51 (2017) 3418–3425, https://doi.org/10.1021/acs.est.6b05623.
[30] K.Y.A. Lin, H.A. Chang, B.J. Chen, Multi-functional MOF-derived magnetic carbon sponge, J. Mater. Chem. A 4 (2016) 13611–13625, https://doi.org/10.1039/c6ta04619c.
[31] W.H. Gu, J.W. Tan, J.B. Chen, Z. Zhang, Y. Zhao, J.W. Yu, G.B. Ji, Multifunctional bulk hybrid foam for infrared stealth, thermal insulation, and microwave absorption, ACS Appl. Mater. Interfaces 12 (2020) 28727–28737, https://doi.org/10.1021/acsami.0c09202.
[32] R.D. Tao, M.J. Qu, S.X. Zhang, F.J. Quan, M. Zhang, W.J. Shen, Y.J. Mei, Preparation of FeOOH supported by melamine sponge and its application for efficient phosphate removal, J. Environ. Chem. Eng. 10 (2022), 108064, https://doi.org/10.1016/j.jece.2022.108064.
[33] H. Qiu, M.C. Ye, Q.Q. Zeng, W.L. Li, J. Fortner, L.L. Liu, L.Y. Yang, Fabrication of agricultural waste supported UiO-66 nanoparticles with high utilization in phosphate removal from water, Chem. Eng. J. 360 (2019) 621–630, https://doi.org/10.1016/j.cej.2018.12.017.
[34] A.D. Eaton, L.S. Clesceri, M.A.H. Franson, E.W. Rice, A.E. Greenberg, Standard Methods for the Examination of Water and Wastewater, 21st ed., American Public Health Association, Washington, DC, 2005.
[35] F.H. Li, J. Jin, Z.Y. Shen, H.S. Ji, M. Yang, Y.M. Yin, Removal and recovery of phosphate and fluoride from water with reusable mesoporous Fe_3O_4@mSiO_2@mLDH composites as sorbents, J. Hazard. Mater. 388 (2020), 121734, https://doi.org/10.1016/j.jhazmat.2019.121734.
[36] A. Bah, Z.Y. Shen, J.N. Yan, F.H. Li, Coupling the batch adsorption enrichment using ternary LDHs with struvite crystallization in a fluidized bed reactor for high-efficiency phosphorus recovery from wastewater, ChemRxiv 2022 (2022), https://doi.org/10.26434/chemrxiv-22022-wwb26435.
[37] A.T. Bah, Z.Y. Shen, J.N. Yan, F.H. Li, Phosphorous recovery from water via batch adsorption enrichment combined with struvite crystallization in a fluidized bed reactor, J. Environ. Chem. Eng. 11 (2023), 110180, https://doi.org/10.1016/j.jece.2023.110180.
[38] M.M. Zhou, J. Li, M. Zhang, H. Wang, Y. Lan, Y.N. Wu, F.T. Li, G.T. Li, A polydopamine layer as the nucleation center of MOF deposition on "inert" polymer surfaces to fabricate hierarchically structured porous films, Chem. Commun. 51 (2015) 2706–2709, https://doi.org/10.1039/c4cc08796h.
[39] Y. Cheng, J.L. Zhang, Facile design of UiO-66-NH_2@La(OH)(3) composite with enhanced efficiency for phosphate removal, J. Environ. Chem. Eng. 9 (2021), 104632, https://doi.org/10.1016/j.jece.2020.104632.
[40] W.S. Zheng, Y. Sun, Y.P. Gu, Assembly of UiO-66 onto Co-doped Fe_3O_4 nanoparticles to activate peroxymonosulfate for efficient degradation of fenitrothion and simultaneous in-situ adsorption of released phosphate, J. Hazard. Mater. 436 (2022), 129058, https://doi.org/10.1016/j.jhazmat.2022.129058.
[41] F.H. Li, W.H. Wu, R.Y. Li, X.R. Fu, Adsorption of phosphate by acid-modified fly ash and palygorskite in aqueous solution: experimental and modeling, Appl. Clay Sci. 132 (2016) 343–352, https://doi.org/10.1016/j.clay.2016.06.028.
[42] Y. Gu, D.H. Xie, Y. Ma, W.X. Qin, H.M. Zhang, G.Z. Wang, Y.X. Zhang, H.J. Zhao, Size modulation of zirconium-based metal organic frameworks for highly efficient phosphate remediation, ACS Appl. Mater. Interfaces 9 (2017) 32151–32160, https://doi.org/10.1021/acsami.7b10024.
[43] T. Liu, S.R. Zheng, L.Y. Yang, Magnetic zirconium-based metal-organic frameworks for selective phosphate adsorption from water, J. Colloid Interface Sci. 552 (2019) 134–141, https://doi.org/10.1016/j.jcis.2019.05.022.
[44] J.W. Zhou, A.V. Ellis, N.H. Voelcker, Recent developments in PDMS surface modification for microfluidic devices, Electrophoresis 31 (2010) 2–16, https://doi.org/10.1002/elps.200900475.
[45] W.H. Chen, Q. Han, Y. Liu, Y.W. Wang, F. Liu, Targeted perfusion adsorption for hyperphosphatemia using mixed matrix microspheres (MMMs) encapsulated NH_2-MIL-101(Fe), J. Mater. Chem. B 9 (2021) 4555–4566, https://doi.org/10.1039/d1tb00329a.
[46] D.L. Sparks, Chapter 7 — Kinetics of soil chemical processes, in: D.L. Sparks (Ed.), Environmental Soil Chemistry, Second edition, Academic Press, Burlington, 2003, pp. 207–244.
[47] J. Lalley, C. Han, X. Li, D.D. Dionysiou, M.N. Nadagouda, Phosphate adsorption using modified iron oxide-based sorbents in lake water: kinetics, equilibrium, and column tests, Chem. Eng. J. 284 (2016) 1386–1396, https://doi.org/10.1016/j.cej.2015.08.114.
[48] Z.F. Wang, E. Nie, J.H. Li, M. Yang, Y.J. Zhao, X.Z. Luo, Z. Zheng, Equilibrium and kinetics of adsorption of phosphate onto iron-doped activated carbon, Environ. Sci. Pollut. Res. 19 (2012) 2908–2917, https://doi.org/10.1007/s11356-012-0799-y.
[49] F.C. Wu, R.L. Tseng, R.S. Juang, Initial behavior of intraparticle diffusion model used in the description of adsorption kinetics, Chem. Eng. J. 153 (2009) 1–8, https://doi.org/10.1016/j.cej.2009.04.042.
[50] D.L. Sparks, Chapter 5 — Sorption phenomena on soils, in: D.L. Sparks (Ed.), Environmental Soil Chemistry, Second edition, Academic Press, Burlington, 2003, pp. 133–186.
[51] N. Kaushik, L.N. Nguyen, J.H. Kim, E.H. Choi, N.K. Kaushik, Strategies for using polydopamine to induce biomineralization of hydroxyapatite on implant materials for bone tissue engineering, Int. J. Mol. Sci. 21 (2020) 6544, https://doi.org/10.3390/ijms21186544.
[52] J.W. Lin, Y.Y. Zhao, Y.H. Zhan, Y. Wang, Influence of coexisting calcium and magnesium ions on phosphate adsorption onto hydrous iron oxide, Environ. Sci. Pollut. Res. 27 (2020) 11303–11319, https://doi.org/10.1007/s11356-020-07676-w.
[53] J. Yang, Y. Dai, X.Y. Zhu, Z. Wang, Y.S. Li, Q.X. Zhuang, J.L. Shi, J.L. Gu, Metal-organic frameworks with inherent recognition sites for selective phosphate sensing through their coordination-induced fluorescence enhancement effect, J. Mater. Chem. A 3 (2015) 7445–7452, https://doi.org/10.1039/c5ta00077g.
[54] T. Guan, Y. Kuang, X.D. Li, J. Fang, W.K. Fang, D.Y. Wu, The recovery of phosphorus from source-separated urine by repeatedly usable magnetic Fe_3O_4@ZrO_2 nanoparticles under acidic conditions, Environ. Int. 134 (2020), 105322, https://doi.org/10.1016/j.envint.2019.105322.
[55] L.J. Wang, X.H. Wen, J. Li, P. Zeng, Y.H. Song, H.Z. Yu, Roles of defects and linker exchange in phosphate adsorption on UiO-66 type metal organic frameworks: influence of phosphate concentration, Chem. Eng. J. 405 (2021), 126681, https://doi.org/10.1016/j.cej.2020.126681.